Cell Reports

Article

Cryo-EM structure of the human TACAN in a closed state

Graphical abstract

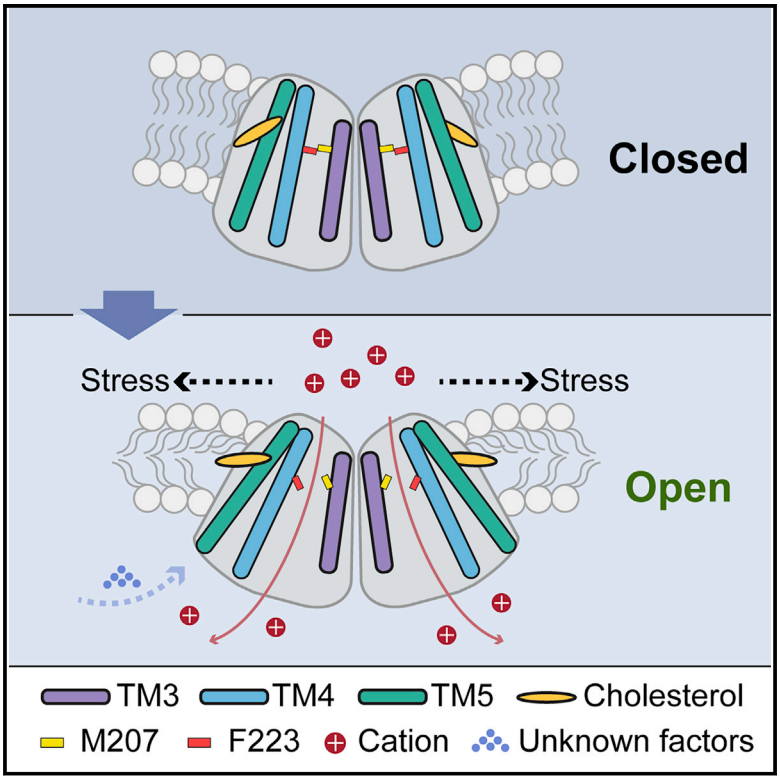

Authors

Xiaozhe Chen, Yaojie Wang, Yang Li, ..., Xing Zhang, Xue Yang, Yuequan Shen

Correspondence

yangxue@nankai.edu.cn (X.Y.), yshen@nankai.edu.cn (Y.S.)

In brief

Chen et al. determine the cryo-EM structure of the human TACAN protein. They demonstrate that human TACAN assembles as a dimer and remains closed at resting state. When activated, it may act as a channel in response to membrane stress.

Highlights

- The cryo-EM structure of human TACAN shows dimer assembly
- Each protomer contains a putative ion conduction pore
- The residue Met207 may act as a gate
- The mutant M207A exhibits obvious currents under membrane pressure

Chen et al., 2022, Cell Reports *38*, 110445
March 1, 2022
https://doi.org/10.1016/j.celrep.2022.110445

CellPress

Cell Reports

CellPress
OPEN ACCESS

Article

Cryo-EM structure of the human TACAN in a closed state

Xiaozhe Chen,[1,2,7] Yaojie Wang,[1,2,7] Yang Li,[1,2,7] Xuhang Lu,[1,2] Jianan Chen,[1,3] Ming Li,[1,2] Tianlei Wen,[1,2] Ning Liu,[1] Shenghai Chang,[4,5] Xing Zhang,[4,5] Xue Yang,[1,2,*] and Yuequan Shen[1,2,6,8,*]

[1]State Key Laboratory of Medicinal Chemical Biology and College of Life Sciences, Nankai University, Tianjin 300350, China
[2]Frontiers Science Center for Cell Responses, Nankai University, Tianjin 300350, China
[3]College of Pharmacy, Nankai University, Tianjin 300350, China
[4]Department of Biophysics and Department of Pathology of Sir Run Run Shaw Hospital, Zhejiang University School of Medicine, Hangzhou 310027, China
[5]Center of Cryo Electron Microscopy, Zhejiang University School of Medicine, Hangzhou 310027, China
[6]Synergetic Innovation Center of Chemical Science and Engineering, Tianjin 300071, China
[7]These authors contributed equally
[8]Lead contact
*Correspondence: yangxue@nankai.edu.cn (X.Y.), yshen@nankai.edu.cn (Y.S.)
https://doi.org/10.1016/j.celrep.2022.110445

SUMMARY

TACAN is an ion channel-like protein that may be involved in sensing mechanical pain. Here, we present the cryo-electron microscopic structure of human TACAN (hTACAN). hTACAN forms a dimer in which each protomer consists of a transmembrane globular domain (TMD) containing six helices and an intracellular domain (ICD) containing two helices. Molecular dynamic simulations suggest that each protomer contains a putative ion conduction pore. A single-point mutation of the key residue Met207 greatly increases membrane pressure-activated currents. In addition, each hTACAN subunit binds one cholesterol molecule. Our data show the molecular assembly of hTACAN and suggest that wild-type hTACAN is in a closed state.

INTRODUCTION

Mechanotransduction, the conversion of mechanical stimuli into electrochemical signals, plays a vital role in all kinds of life forms. The primary sensors that react quickly to mechanical signals are mechanosensitive ion channels (MSCs) (Douguet and Honore, 2019; Jin et al., 2020; Kefauver et al., 2020). A variety of MSC families, including mechanosensitive channel large conductance (MscL) (Cox et al., 2018), two-pore potassium (K2P) channels (Brohawn et al., 2014), piezos (Murthy et al., 2017), osmosensitive calcium-permeable cation (OSCA) channels (Yuan et al., 2014), and transmembrane channel-like protein 1/2 (TMC1/2) (Jia et al., 2020), have been identified. Each has a unique structure and function (Kefauver et al., 2020). These channels are involved in several physiological functions, such as hearing, touch, pain, and proprioception (Douguet and Honore, 2019; Jin et al., 2020; Naismith and Booth, 2012).

Pain is a biological warning signal that is detected by nociceptors that are activated by multiple environmental factors. It is sensed by the opening of several types of MSCs, including piezos in mammals (Arenas and Lumpkin, 2020; Beaulieu-Laroche et al., 2020). It has been shown that piezos are associated with the sensation of touch and mechanical allodynia (Murthy et al., 2017). A recent study reported that the transmembrane protein 120A, referred to as TACAN, is a possible novel ion channel responsible for sensing acute mechanical pain (Beaulieu-Laroche et al., 2020) and is involved in mechanically sensitive nociception and mechanical pain perception currents in mice (Bonet et al., 2020).

TACAN is conserved in vertebrates and shares no sequence homology with other membrane proteins. It was originally identified as a nuclear envelope protein (Malik et al., 2010) and may be involved in adipocyte differentiation (Batrakou et al., 2015). TACAN contains 343 amino acids (aa) and consists of 6 transmembrane helices with intracellular amino and carboxyl termini (Beaulieu-Laroche et al., 2020). To better understand its domain organization and channel assembly, we determined the structure of human TACAN (hTACAN) using single-particle cryoelectron microscopy (cryo-EM).

RESULTS

Structure determination

Structural studies of full-length hTACAN were performed by cryo-EM single-particle analysis. The purified hTACAN protein showed a monodisperse peak (approximately corresponding to a dimer) on the analytical size-exclusion column (Figure S1A). The peak fraction was then collected and concentrated for cryo-EM sample preparation (Figure S1B). The 2-dimensional (2D) class average suggested that the protein is a dimer with 2-fold symmetry (Figure S1C). Subsequent 3D reconstructions of hTACAN were determined at an overall resolution of 3.66 Å (Figures S1D–S1G). The electron density maps for most amino acid side chains of hTACAN are clearly resolvable (Figure S1H), allowing

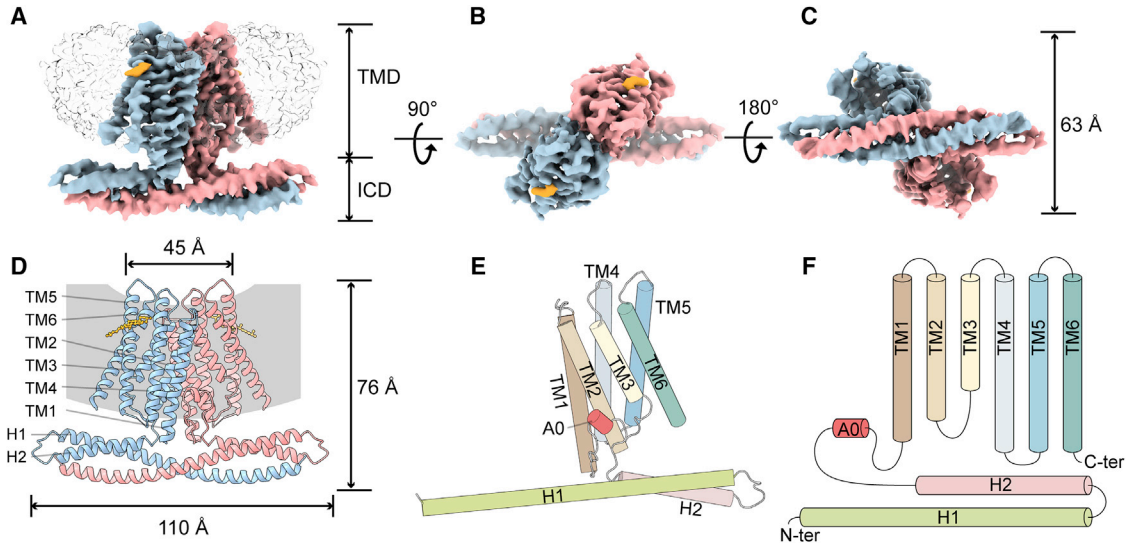

Figure 1. The overall structure of hTACAN

(A–C) Side (A), top (B), and bottom (C) views of a cryo-EM density map. The two protomers are blue and pink, respectively. The density of cholesterol is yellow. The two globular domains of hTACAN are buried in the detergent micelles represented by the transparent gray map. See also Figure S1.

(D and E) Illustrations of the hTACAN dimer (D) and the hTACAN protomer (E).

(F) Schematic illustration outlining the protein secondary structures of one hTACAN protomer. See also Figure S2.

See also Figure S3 and Video S1.

for accurate model building. The final model included most amino acids except the N-terminal region (aa 1–7), disordered loop (aa 249–263), and C-terminal region (aa 336–343).

Overall structure

The overall structure of hTACAN assembles as a dimer with a 2-fold rotation axis perpendicular to the membrane bilayer (Figures

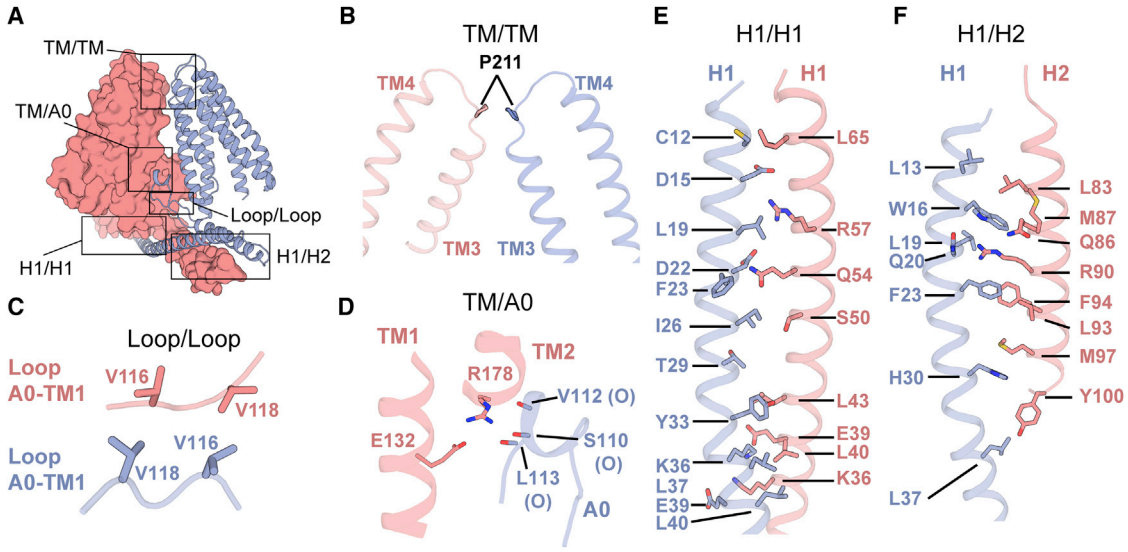

Figure 2. Intersubunit interfaces

(A) Side view of the overall illustration of the intersubunit interactions. Two protomers are shown in the surface representation (pink) and illustration (blue).

(B) The interaction between two TM3 helices at residue Pro211.

(C) Interactions between two loops. Loop A0-TM1 denotes that the loop is located between the A0 helix and the TM1 helix in each protomer.

(D) Interactions between the TM2 helix and the A0 helix. The side chain of R178 forms hydrogen bonds with main chain oxygen atoms from three residues: S110, V112, and L113.

(E and F) Interactions between two H1 helices (E) and between helix H1 and helix H2 (F).

All of the interactions described in (C)–(F) are reciprocal.

See also Figure S4.

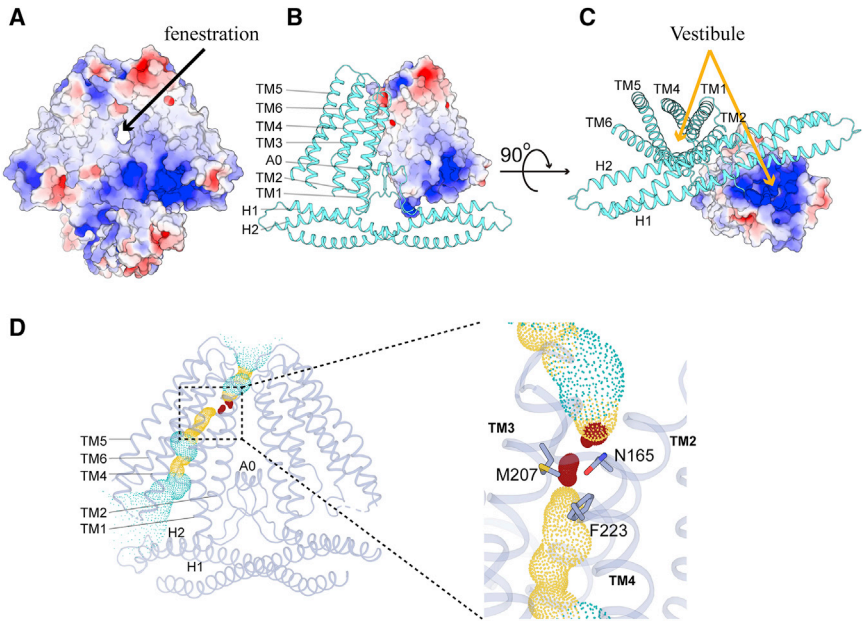

Figure 3. Pore of hTACAN

(A) Surface potential map of the hTACAN proteins. The hTACAN proteins in the surface representation are colored according to electrostatic surface potentials from −5 to 5 kT/e (red to blue).

(B and C) Vestibule inside one protomer of the hTACAN protein. The TM domain of one protomer is shown in the surface presentation.

(D) Potential ion conduction pore inside one protomer. The snapshot is the last frame of a 200-ns MD simulation without surface tension. This simulation is repeated 3 times. The constriction region of the pore is magnified on the right side. The dots colored blue, red, and orange represent the pathways of the pore. Red, pore radius is <1.15 Å; yellow, pore radius ranges from 1.15 to 2.3 Å; cyan, pore radius is >2.3 Å.

See also Figure S5.

1A–1C). It forms a two-layer architecture: the upper transmembrane part (called the transmembrane globular domain [TMD]) consists of two globular domains, and the lower cytosolic part (called the intracellular domain [ICD]) consists of domain-swapped four-helix bundles (Figure 1D). Two sterol molecules were identified on two sides of the dimer (Figure 1D). Each globular domain is buried in the membrane bilayer and contains six transmembrane helices called TM1–TM6 and a small anchoring helix called A0 (Figures 1E, 1F, and S2A). The anchoring helix is reminiscent of the anchor domain in the piezo channels (Saotome et al., 2018; Wang et al., 2019; Zhao et al., 2018). It is located in the dimeric interface and may contribute to the stabilization of the dimer. The ICD of each protomer contains two helices called H1 and H2. H1 forms an extra-long helix extending to the other protomer, resulting in the N-terminal half of H1 in one protomer interacting with the C-terminal half of H1 and the entire H2 of the other protomer. It has been noted that our hTACAN structure is highly similar to the recently published hTACAN structures (Niu et al., 2021; Rong et al., 2021; Xue et al., 2021) (Figures S2B–S2D). Dali screening (http://ekhidna2.biocenter.helsinki.fi/dali/) showed that the transmembrane domain of the hTACAN monomer is similar to the human elongation of very-long-chain fatty acids protein 7 (hELOVL7). However, the dimer assembly between the two proteins differed in 2-fold symmetry and monomer orientation (Figure S3A).

Compared with previously published mechanosensitive ion channels, hTACAN shares a dimeric architecture with *Arabidopsis thaliana* OSCA (AtOSCA) (Jojoa-Cruz et al., 2018; Zhang et al., 2018), despite having no sequence homology to this protein, while the topologies of the protomers of hTACAN and AtOSCA are completely different (Figures S3B and S3C). Each protomer of the AtOSCA contains 11 TMs, while the hTACAN has only 6 TMs. In addition, the beam domain (Saotome et al., 2018; Zhao et al., 2018) or the beam-like domain (Jojoa-Cruz et al., 2018), which connects to pore-lining helices and plays an important role in gating the piezo channel or the AtOSCA, is absent in our hTACAN structure. Moreover, the intersubunit cleft of AtOSCA is sufficiently wide to be filled with phospholipid molecules (Jojoa-Cruz et al., 2018), while the intersubunit cleft of hTACAN is too narrow to accommodate phospholipid molecules, as shown by molecular dynamics simulations (Figures S3D–S3F; Video S1). These results suggest that if hTACAN forms a channel, it would have a novel mechanogating mechanism.

Intersubunit interactions

Interactions of the two hTACAN protomers occur at both the TMD interface and the ICD interface (Figure 2A). Due to the presence of the 2-fold symmetry axis, all of the interactions between the two protomers are reciprocal. The TMD interface can be further divided into the TM/TM interface (Figure 2B), the loop A0-TM1/loop A0-TM1 interface (Figure 2C), and the TM/A0 interface (Figure 2D). The TM/TM interface contains one hydrophobic pair interaction between two prolines (P211) of TM3 from each protomer. The loop A0-TM1/loop A0-TM1 interface is involved in the hydrophobic interactions between residue V116 of one protomer and residue V118 of another protomer. The TM/A0 interface includes three hydrogen bonds mediated by residue R178 of TM2 from one protomer and three main chain oxygen atoms of S110, V112, and L113 of the other protomer. The ICD interface contains extensive interactions between two H1 helices from each protomer (Figure 2E) and between helix H1 from one protomer and helix H2 from another protomer (Figure 2F).

To further confirm the intersubunit interactions, we performed a coimmunoprecipitation (coIP) experiment. We constructed three truncation mutants: delta-halfH1 (residues 43–343), delta-H1 (residues 75–343), and delta-ICD (residues 101–343). C-terminal FLAG or GFP tags were added to these mutant proteins. Then, the mutant plasmids with two different tags were co-transfected into HEK293T cells for coIP. Our results showed that the deletion of H1 significantly attenuated dimeric assembly, suggesting that dimeric hTACAN requires the integrity of the ICD (Figure S4).

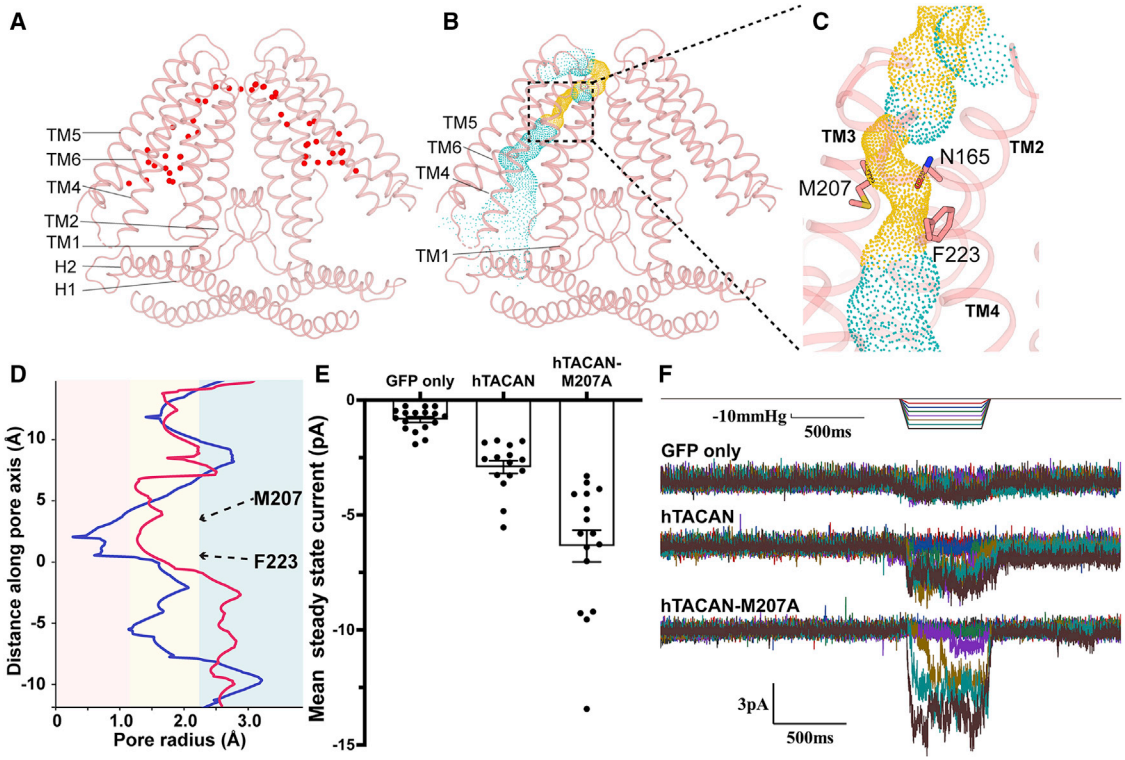

Figure 4. Ion conduction pathway

(A) A representative snapshot of the continuous water channel in the hTACAN dimer with a surface tension of 35 mN/m in a 200-ns MD simulation. This simulation is repeated 3 times. The red dots denote water molecules. The illustration of the hTACAN dimer is shown in pink. See Figure S5 and Video S2.

(B) The snapshot is the last frame of the 200-ns MD simulation with a surface tension of 35 mN/m. This simulation is repeated 3 times. The dots colored blue, red, and orange represent the pathways of the pore. Red, pore radius is <1.15 Å; yellow, pore radius ranges from 1.15 to 2.3 Å; cyan, pore radius is >2.3 Å. The illustration of the hTACAN dimer is shown in pink. See Figure S5.

(C) An enlarged view of the restricted area in the pore. The side chains of the two residues M207 and F223 form a hydrophobic gate. Residues N165, M207, and F223 are shown in the stick model.

(D) Pore radius profile of hTACAN wild-type dimer in a 200-ns MD simulation without (blue) or with 35 mN/m (red) surface tension. Each simulation is repeated 3 times. For clarity, two representative curves are shown. Profiles of pore radius in a total of 6 simulations are shown in Figure S5B.

(E) Mean currents recorded (−80 mV) in response to −70 mm Hg pressure for individual cells expressing wild-type hTACAN (n = 15) or mutant M207A (n = 16) or mock (GFP only, n = 17). n is the number of cells. The data are represented as mean ± SEM. See Figure S5.

(F) Representative traces of one COS-7 cell expressing wild-type hTACAN or GFP only (mock) or hTACAN-M207A using a cell-attached configuration in response to different membrane pressures at −80 mV. The color of each trace corresponds to the color of various membrane pressures. Replicates are the same as described in (E).

See also Figure S6 and Video S3.

Ion-conduction pathway

The surface map of the hTACAN dimer shows that there is a large fenestration in the middle of the intersubunit cleft from the side view (Figure 3A). Protein atoms occupied spaces around the fenestration. Therefore, the intersubunit cleft is unlikely to act as an ion-conducting pathway. Instead, a vestibule toward the intracellular side was identified. This vestibule is positively charged in the protomer according to the surface potential map (Figures 3B and 3C). However, at the extracellular side, it is difficult to find an opening to connect with this large vestibule to act as a putative ion-conducting pathway in our current structure. We therefore conducted molecular dynamics (MD) simulations. Three replicas of the 200-ns simulation were performed (Figure S5A) and the results showed that no continuous distribution of water passages was found within each subunit (Figure 3D), indicating that our hTACAN structure represents a nonconducting state. To investigate the conformational changes occurring in hTACAN in response to mechanical stress, different surface tensions were applied to the lipid bilayer during the atomic MD simulations (Figure S5A). The simulation system remains stable at a maximal surface tension of 35 mN/m, which is used in the following studies unless otherwise specified. After a surface tension of 35 mN/m was applied to the system, water molecules were able to spontaneously form a continuous channel from the extracellular side to the intracellular side in each protomer (Figure 4A; Video S2). The corresponding ion conduction pathways were calculated by the HOLE program (Smart et al., 1996) (Figure 4B). The restriction region of the ion-conduction pathway was composed of three residues: N165 of TM2, M207 of TM3, and F223 of TM4 (Figure 4C). Specifically, the side chains of M207 and F223 undergo large

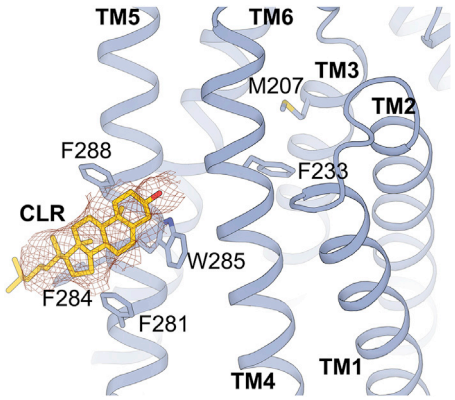

Figure 5. Binding of cholesterol molecules to hTACAN

The binding site for cholesterol (CLR) on TM5. hTACAN is shown in blue and the CLR molecule is shown in yellow. The EM density map of the CLR molecule is represented by red meshed lines, and the side chains of residues involved in CLR binding (F281, F284, W285, and F288) are shown as stick models. The residues involved in pore formation (M207 and F223) are also shown in the stick model to show their positions relative to the CLR molecule.
See also Figure S7.

conformational changes before and after surface tension in MD simulations. As shown in Figures 4D and S5B, in response to the surface tension, the restriction area increases to a more dilated state. To verify the ion-conduction pathway, we conducted electrophysiological studies. GFP only (mock), GFP-tagged wild-type hTACAN, and GFP-tagged mutant M207A plasmids were transiently transfected into COS-7 cells, and the cell-attached configuration mode was then applied. A cell-surface biotinylation assay showed that the surface expression levels of the mutant M207A were similar to those of the wild type (Figure S5C). Compared with mock, the currents measured in response to different membrane pressures for wild-type hTACAN were not markedly different, while the currents for the mutant M207A showed an approximately 6-fold increase (Figures 4E, 4F, and S5D). To cross-validate the mutant M207A effect, we carried out MD simulations for the mutant M207A in response to the surface tension. Compared with the wild type, the mutant M207A was indeed more permeable to water molecules in response to a surface tension of 35 mN/m (Figure S6; Videos S2 and S3). Therefore, it seems that wild-type hTACAN is in a closed state, and other unknown factors may be required to activate the hTACAN protein.

Cholesterol binding

In the hTACAN structure, we observed a robust density that fits well with the cholesterol molecule at the flanks of the two protomers (Figures 1A, 1B, 1D, and 5). Mass spectrometry identified the major peak of the molecular weight of 387 Da, which corresponds to the cholesterol (Figure S7A), from the purified hTACAN protein sample. No other lipid molecules were identified in our experiment. The hydrophobic steroid nucleus of cholesterol is stabilized by multiple residues with bulky hydrophobic side chains, including F281, F284, W285, and F288 of TM5 (Figure 5). We then made the mutant hTACAN F284A-W285A-F288A. The subsequent mass spectrometry analysis of the purified mutant protein sample did not find the cholesterol peak (Figure S7B). Although cholesteryl hemisuccinate (CHS, cholesterol-mimicking detergent) was used in protein sample purification, we did not find the peak corresponding to the CHS molecule in the mass spectrometry analysis. Moreover, phospholipid molecules have been shown to be bound in multiple mechanosensitive channels and to be involved in their activation (Kefauver et al., 2020). However, phospholipid molecules have not been found in our current TACAN structure. These results suggest that cholesterol is a specific binding molecule for the hTACAN protein. The functional role cholesterol plays in hTACAN needs to be clarified further.

DISCUSSION

Our studies described here showed that hTACAN may represent a structurally novel class of ion channels. Although its topology is different, the dimeric architecture and ion conduction pathway of hTACAN are reminiscent of those of AtOSCAs, suggesting that these two pressure-activated mechanosensitive channels may share some commonalities upon activation. Importantly, cholesterols were identified in the TACAN protein, which, to the best of our knowledge, has never been found in any known mechanosensitive channel.

Recently, authors in the published literature have argued that the TACAN may be a coenzyme A-binding protein rather than a mechanosensitive channel (Niu et al., 2021; Rong et al.,

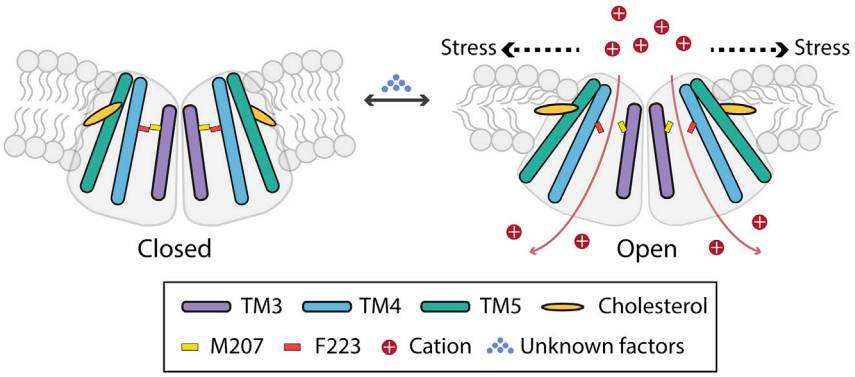

Figure 6. Putative opening mechanism of hTACAN under mechanical stress

Residue M207 on TM3 and residue F223 on TM4 form a gate that keeps hTACAN closed in a resting state. When hTACAN senses membrane stress, the movement of TM3 and TM4 causes the movement of M207 and F223, thus opening the gate. The cations then flow through the channel. Some unknown factors may be required in this process.

2021; Xue et al., 2021). They have shown that a coenzyme A molecule is bound in the vestibule of the membrane domain of hTACAN and that the expression of hTACAN was not sufficient to mediate mechanosensitive currents in cells. However, these results may suggest that the wild-type hTACAN is in a closed state due to the binding of coenzyme A to block ion conduction. Additional subunits may be required to release coenzyme A to activate hTACAN. In other words, there is a possibility that functional hTACAN contains multiple subunits. Mechanosensitive channels can be made up of several subunits. For example, in hair cells, mechanoelectrical transduction channels consist of TMC1/2, transmembrane inner ear (TMIE), and transmembrane proteins lipoma HMGIC fusion partner-like 5 (TMHS/LHFPL5) and may be more abundant (Al-Sheikh and Kang, 2020).

Our results seem to be consistent with this hypothesis. In our hTACAN structure, we did not find any densities corresponding to coenzyme A, indicating that the binding of coenzyme A to hTACAN may be dynamic. Moreover, our MD and electrophysiology data showed that residue M207 seems to act as a gate to block the putative ion conduction pathway in wild-type hTACAN. The single-point mutation of M207A made hTACAN more permeable.

We propose that other unknown factors may be involved in the movement of helices TM3 and TM4, thus eliciting the shift of the side chains of two hydrophobic residues (F223 and M207) to open hTACAN (Figure 6). Further studies are required to understand the detailed conformational transition during activation, but our structure of hTACAN in a closed state will be helpful for the future investigation of hTACAN in a constitutively active state and contribute to the development of a novel class of painkillers.

Limitations of the study

Although we used MD simulations to identify the putative ion conduction pathway of hTACAN, and applied electrophysiological techniques to show that the residue Met207 may act as a gate, the lack of specific hTACAN inhibitors still limits our further verification of the characteristics of the hTACAN channel. It is hoped that small molecules or antibodies against the extracellular pores of hTACAN can be developed in the future, which will further determine whether hTACAN can induce membrane pressure responsive currents. In addition, since we reported the hTACAN structure in the closed state, the gating mechanism we currently propose is largely hypothetical. If the hTACAN structure in the open state can be captured, then the gating mechanism of the channel can really be clarified. Finally, we found that cholesterol specifically binds to hTACAN protein, which is completely different from other known mechanically sensitive channels. If an activator of hTACAN protein can be found in the future, the regulation of hTACAN protein by cholesterol can be elaborated.

STAR★METHODS

Detailed methods are provided in the online version of this paper and include the following:

- KEY RESOURCES TABLE
- RESOURCE AVAILABILITY
  - Lead contact
  - Materials availability
  - Data and code availability
- EXPERIMENTAL MODEL AND SUBJECT DETAILS
- METHODS DETAILS
  - Plasmid
  - Protein expression and purification
  - Cryo-EM sample preparation
  - Image processing
  - Model building and refinement
  - Co-immunoprecipitation
  - Cell surface biotinylation assay
  - Electrophysiology
  - Cross-linking experiment
  - Coarse-grained MD simulations
  - All-atom MD simulations
  - Liquid chromatography–mass spectrometry (LC–MS)
- QUANTIFICATION AND STATISTICAL ANALYSIS

SUPPLEMENTAL INFORMATION

Supplemental information can be found online at https://doi.org/10.1016/j.celrep.2022.110445.

ACKNOWLEDGMENTS

We thank Prof. B. Xiao at Tsinghua University for help in the electrophysiology studies; the technical assistance in the Center of Cryo-Electron Microscopy (CCEM), Zhejiang University on Cryo-EM for data acquisition; Dr. J. Lu and Dr. A. Li for the support in the electron microscopy at Nankai University; and Dr. Q. Wang for the support in the mass spectrometry facilities at Nankai University. This work was supported by the National Key Research and Development Program of China (grant 2017YFA0504801 to Y.S.; 2017YFA0504803 and 2018YFA0507700 to X.Z.), the National Natural Science Foundation of China (grants 91954119 and 31870736 to X.Y.; grants 32071231 and 31870834 to Y.S.), the Fundamental Research Funds for the Central Universities (2018XZZX001-13 to X.Z.), and the Fund Program of Talent Training in Nankai University (035-BB042112 to X.Y).

AUTHOR CONTRIBUTIONS

X.C. performed the protein expression, purification, sample preparation, and cryo-EM data collection; Y.W. performed the electrophysiology experiment; Y.L. performed the MD simulations; J.C., M.L., and T.W. performed the protein expression and purification; X.L., S.C., X.Z., and X.Y. performed the cryo-EM data collection; X.Y. conducted the cryo-EM reconstruction; N.L. performed the mass spectrometry analysis; X.C., Y.W., Y.L., X.Y., and Y.S. analyzed the data, designed the study, and wrote the paper. All of the authors discussed the results and commented on the manuscript.

DECLARATION OF INTERESTS

The authors declare no competing interests.

Received: September 6, 2021
Revised: December 17, 2021
Accepted: February 4, 2022
Published: March 1, 2022

REFERENCES

Al-Sheikh, U., and Kang, L. (2020). Molecular crux of hair cell mechanotransduction machinery. Neuron *107*, 404–406.

Anandakrishnan, R., Aguilar, B., and Onufriev, A.V. (2012). H++ 3.0: automating pK prediction and the preparation of biomolecular structures for atomistic molecular modeling and simulations. Nucleic Acids Res. *40*, W537–W541.

Arenas, O.M., and Lumpkin, E.A. (2020). Touching base with mechanical pain. Cell *180*, 824–826.

Batrakou, D.G., de Las Heras, J.I., Czapiewski, R., Mouras, R., and Schirmer, E.C. (2015). TMEM120A and B: nuclear envelope transmembrane proteins important for adipocyte differentiation. PLoS One *10*, e0127712.

Beaulieu-Laroche, L., Christin, M., Donoghue, A., Agosti, F., Yousefpour, N., Petitjean, H., Davidova, A., Stanton, C., Khan, U., Dietz, C., et al. (2020). TACAN is an ion channel involved in sensing mechanical pain. Cell *180*, 956–967.e17.

Berendsen, H.J.C.P., Postma, J., Gunsteren, W., Dinola, A.D., and Haak, J.R. (1984). Molecular-dynamics with coupling to an external bath. J. Chem. Phys. *81*, 3684.

Bonet, I.J.M., Araldi, D., Bogen, O., and Levine, J.D. (2020). Involvement of TACAN, a mechanotransducing ion channel, in inflammatory but not neuropathic hyperalgesia in the rat. J. Pain *22*, 498–508.

Brohawn, S.G., Campbell, E.B., and MacKinnon, R. (2014). Physical mechanism for gating and mechanosensitivity of the human TRAAK K+ channel. Nature *516*, 126–130.

Bussi, G., Donadio, D., and Parrinello, M. (2007). Canonical sampling through velocity rescaling. J. Chem. Phys. *126*, 014101.

Cox, C.D., Bavi, N., and Martinac, B. (2018). Bacterial mechanosensors. Annu. Rev. Physiol. *80*, 71–93.

Darden, T., York, D., and Pedersen, L. (1993). Particle mesh Ewald: an N-log (N) method for Ewald sums in large systems. J. Chem. Phys. *98*, 10089–10092.

Dickson, C.J., Madej, B.D., Skjevik, A.A., Betz, R.M., Teigen, K., Gould, I.R., and Walker, R.C. (2014). Lipid14: the amber lipid force field. J. Chem. Theory Comput. *10*, 865–879.

Douguet, D., and Honore, E. (2019). Mammalian mechanoelectrical transduction: structure and function of force-gated ion channels. Cell *179*, 340–354.

Emsley, P., and Cowtan, K. (2004). Coot: model-building tools for molecular graphics. Acta Crystallogr. D Biol. Crystallogr. *60*, 2126–2132.

Hess, B., Bekker, H., Berendsen, H., and Fraaije, J. (1998). LINCS: a linear constraint solver for molecular simulations. J. Comput. Chem. *18*, 1463–1472.

Humphrey, W., Dalke, A., and Schulten, K. (1996). VMD: visual molecular dynamics. J. Mol. Graph. Model. *14*, 33–38.

Jia, Y., Zhao, Y., Kusakizako, T., Wang, Y., Pan, C., Zhang, Y., Nureki, O., Hattori, M., and Yan, Z. (2020). TMC1 and TMC2 proteins are pore-forming subunits of mechanosensitive ion channels. Neuron *105*, 310–321.

Jin, P., Jan, L.Y., and Jan, Y.N. (2020). Mechanosensitive ion channels: structural features relevant to mechanotransduction mechanisms. Annu. Rev. Neurosci. *43*, 207–229.

Jojoa-Cruz, S., Saotome, K., Murthy, S.E., Tsui, C.C.A., Sansom, M.S., Patapoutian, A., and Ward, A.B. (2018). Cryo-EM structure of the mechanically activated ion channel OSCA1.2. eLife *7*, e41845.

Jones, D.T. (1999). Protein secondary structure prediction based on position-specific scoring matrices. J. Mol. Biol. *292*, 195–202.

Jong, D.D., Singh, G., Bennett, W., Arnarez, C., Wassenaar, T.A., SchaFer, L.V., Periole, X., Tieleman, D.P., and Marrink, S.J. (2013). Improved parameters for the Martini coarse-grained protein force field. J. Chem. Theor. Comput. *9*, 687–697.

Kefauver, J.M., Ward, A.B., and Patapoutian, A. (2020). Discoveries in structure and physiology of mechanically activated ion channels. Nature *587*, 567–576.

Kucukelbir, A., Sigworth, F.J., and Tagare, H.D. (2014). Quantifying the local resolution of cryo-EM density maps. Nat. Methods *11*, 63–65.

Liebschner, D., Afonine, P.V., Baker, M.L., Bunkoczi, G., Chen, V.B., Croll, T.I., Hintze, B., Hung, L.W., Jain, S., McCoy, A.J., et al. (2019). Macromolecular structure determination using X-rays, neutrons and electrons: recent developments in Phenix. Acta Crystallogr. D Struct. Biol. *75*, 861–877.

Maier, J.A., Martinez, C., Kasavajhala, K., Wickstrom, L., Hauser, K.E., and Simmerling, C. (2015). ff14SB: improving the accuracy of protein side chain and backbone parameters from ff99SB. J. Chem. Theor. Comput. *11*, 3696–3713.

Malik, P., Korfali, N., Srsen, V., Lazou, V., Batrakou, D.G., Zuleger, N., Kavanagh, D.M., Wilkie, G.S., Goldberg, M.W., and Schirmer, E.C. (2010). Cell-specific and lamin-dependent targeting of novel transmembrane proteins in the nuclear envelope. Cell. Mol. Life Sci. *67*, 1353–1369.

Murthy, S.E., Dubin, A.E., and Patapoutian, A. (2017). Piezos thrive under pressure: mechanically activated ion channels in health and disease. Nat. Rev. Mol. Cell Biol. *18*, 771–783.

Naismith, J.H., and Booth, I.R. (2012). Bacterial mechanosensitive channels–MscS: evolution's solution to creating sensitivity in function. Annu. Rev. Biophys. *41*, 157–177.

Niu, Y., Tao, X., Vaisey, G., Olinares, P.D.B., Alwaseem, H., Chait, B.T., and MacKinnon, R. (2021). Analysis of the mechanosensor channel functionality of TACAN. eLife *10*, e71188.

Pall, S., Zhmurov, A., Bauer, P., Abraham, M., Lundborg, M., Gray, A., Hess, B., and Lindahl, E. (2020). Heterogeneous parallelization and acceleration of molecular dynamics simulations in GROMACS. J. Chem. Phys. *153*, 134110.

Pastor, R.W., Brooks, B.R., and Szabo, A. (1988). An analysis of the accuracy of Langevin and molecular dynamics algorithms. Mol. Phys. *65*, 1409–1419.

Periole, X., Cavalli, M., Marrink, S.J., and Ceruso, M.A. (2009). Combining an elastic network with a coarse-grained molecular force field: structure, dynamics, and intermolecular recognition. J. Chem. Theor. Comput. *5*, 2531–2543.

Pettersen, E.F., Goddard, T.D., Huang, C.C., Couch, G.S., Greenblatt, D.M., Meng, E.C., and Ferrin, T.E. (2004). UCSF Chimera–a visualization system for exploratory research and analysis. J. Comput. Chem. *25*, 1605–1612.

Punjani, A., Rubinstein, J.L., Fleet, D.J., and Brubaker, M.A. (2017). cryoSPARC: algorithms for rapid unsupervised cryo-EM structure determination. Nat. Methods *14*, 290–296.

Rohou, A., and Grigorieff, N. (2015). CTFFIND4: fast and accurate defocus estimation from electron micrographs. J. Struct. Biol. *192*, 216–221.

Rong, Y., Jiang, J., Gao, Y., Guo, J., Song, D., Liu, W., Zhang, M., Zhao, Y., Xiao, B., and Liu, Z. (2021). TMEM120A contains a specific coenzyme A-binding site and might not mediate poking- or stretch-induced channel activities in cells. eLife *10*, e71474.

Ryckaert, J.-P., Ciccotti, G., and Berendsen, H.J.C. (1977). Numerical integration of the Cartesian equations of motion of a system with constraints: molecular dynamics of N-alkanes. J. Comput. Phys. *23*, 327–341.

Saotome, K., Murthy, S.E., Kefauver, J.M., Whitwam, T., Patapoutian, A., and Ward, A.B. (2018). Structure of the mechanically activated ion channel Piezo1. Nature *554*, 481–486.

Smart, O.S., Neduvelil, J.G., Wang, X., Wallace, B.A., and Sansom, M.S. (1996). HOLE: a program for the analysis of the pore dimensions of ion channel structural models. J. Mol. Graph. *14*, 354–360.

Takaba, K., Maki-Yonekura, S., and Yonekura, K. (2020). Collecting large datasets of rotational electron diffraction with ParallEM and SerialEM. J. Struct. Biol. *211*, 107549.

Wang, L., Zhou, H., Zhang, M., Liu, W., Deng, T., Zhao, Q., Li, Y., Lei, J., Li, X., and Xiao, B. (2019). Structure and mechanogating of the mammalian tactile channel PIEZO2. Nature *573*, 225–229.

Wassenaar, T.A., Ingolfsson, H.I., Boeckmann, R.A., Tieleman, D.P., and Marrink, S.J. (2015). Computational lipidomics with insane: a versatile tool for generating custom membranes for molecular simulations. J. Chem. Theory Comput. *11*, 2144–2155.

Wassenaar, T.A., Pluhackova, K., B?Ckmann, R.A., Marrink, S.J., and Tieleman, D.P. (2014). Going backward: a flexible geometric approach to reverse transformation from coarse grained to atomistic models. J. Chem. Theory Comput. *10*, 676–690.

Xue, J., Han, Y., Baniasadi, H., Zeng, W., Pei, J., Grishin, N.V., Wang, J., Tu, B.P., and Jiang, Y. (2021). TMEM120A is a coenzyme A-binding membrane protein with structural similarities to ELOVL fatty acid elongase. eLife *10*, e71220.

Yuan, F., Yang, H., Xue, Y., Kong, D., Ye, R., Li, C., Zhang, J., Theprungsirikul, L., Shrift, T., Krichilsky, B., et al. (2014). OSCA1 mediates osmotic-stress-evoked Ca2+ increases vital for osmosensing in Arabidopsis. Nature *514*, 367–371.

Zhang, M., Wang, D., Kang, Y., Wu, J.X., Yao, F., Pan, C., Yan, Z., Song, C., and Chen, L. (2018). Structure of the mechanosensitive OSCA channels. Nat. Struct. Mol. Biol. *25*, 850–858.

Zhao, Q., Zhou, H., Chi, S., Wang, Y., Wang, J., Geng, J., Wu, K., Liu, W., Zhang, T., Dong, M.Q., et al. (2018). Structure and mechanogating mechanism of the Piezo1 channel. Nature *554*, 487–492.

Zheng, S.Q., Palovcak, E., Armache, J.P., Verba, K.A., Cheng, Y., and Agard, D.A. (2017). MotionCor2: anisotropic correction of beam-induced motion for improved cryo-electron microscopy. Nat. Methods *14*, 331–332.

Zivanov, J., Nakane, T., Forsberg, B.O., Kimanius, D., Hagen, W.J., Lindahl, E., and Scheres, S.H. (2018). New tools for automated high-resolution cryo-EM structure determination in RELION-3. eLife *7*, e42166.

STAR★METHODS

KEY RESOURCES TABLE

REAGENT or RESOURCE	SOURCE	IDENTIFIER
Antibodies		
Mouse monoclonal anti-GFP	Abcam	Cat#ab1218; RRID: AB_298911
Mouse monoclonal anti-FLAG	Sigma -Aldrich	Cat#F1804-5MG, RRID: AB_262044
Bacterial and virus strains		
Trans1-T1 Phage Resistant Chemically Competent Cell	TransGen	Cat#CD501-01
DH10Bac *Escherichia coli* strain	Thermo Fisher	Cat#10361012
Chemicals, peptides, and recombinant proteins		
Polyethylenimine, Linear (MW25,000)	Polysciences, Inc	Cat#23966-2
Protease inhibitor cocktail	TargetMol	Cat# C0001
X-tremeGENE HP DNA	Roche	Cat# 6366546001
biotinamidohexanoic acid 3-sulfo-N-hydroxysuccinimide ester sodium salt	Sigma	Cat# B1022
cholesteryl hemisuccinate (CHS)	Sigma	Cat# C6512-5G
n-Dodecyl-β-D-Maltopyranoside (DDM)	Anatrace	Cat#D310
Disuccinimidyl Suberate	Thermo Fisher	Cat#21555
glycol-diosgenin (GDN)	Anatrace	Cat#GDN101
lauryl maltose neopentyl glycol (LMNG)	Anatrace	Cat#NG310
NeutrAvidin agarose	Thermo Fisher	Cat# 29201
DMEM	Sigma	Cat#D5648
Fetal Bovine Serum	PAN-Seratech	Cat#ST30-3302
Freestyle 293 medium	GIBCO	Cat# 12338-018
Insect-XPRESS	Lonza BioWhittaker	Cat#12-730Q
Critical commercial assays		
Plasmid Miniprep Kit	Axygen	Cat#AP-MN-P-250
Gel Extraction Kit	CWBIO	Cat#CW2302M
Superose 6, 10/300 GL	GE Healthcare	Cat# 17-5172-01
Anti-DYKDDDDK Tag (L5) Affinity Gel Antibody	Biolegend	Cat#651503
GFP-Trap Agrose	ChromoTek	Cat# gta-100
Deposited data		
Coordinates of human TACAN	This paper	PDB: 7F6V
Cryo-EM map of human TACAN	This paper	EMD: 31482
Experimental models: Cell lines		
Human Embryonic Kidney HEK293S-GnTi cell line	Laboratory of Professor Jun Liao from niversity of Shanghai for Science and Technology	N/A
Human Embryonic Kidney HEK293T cell line	ATCC	CRL-11268
Spodoptera frugiperda Sf9 cells	Laboratory of Professor Xinquan Wang from Tsinghua University	N/A
African green monkey kidney COS-7 cell line	Laboratory of Professor Junjie Hu from Institute of Biophysics, Chinese Academy of Science	N/A
Recombinant DNA		
pcDNA-hTACAN-HIS-GFP	This paper	N/A

(*Continued on next page*)

Continued

REAGENT or RESOURCE	SOURCE	IDENTIFIER
pcDNA-hTACAN-FLAG	This paper	N/A
pcDNA-hTACAN delta-halfH1-GFP	This paper	N/A
pcDNA-hTACAN delta-H1-GFP	This paper	N/A
pcDNA-hTACAN delta-ICD-GFP	This paper	N/A
pcDNA-hTACAN delta-halfH1-FLAG	This paper	N/A
pcDNA-hTACAN delta-H1-FLAG	This paper	N/A
pcDNA-hTACAN delta-ICD-FLAG	This paper	N/A
Software and algorithms		
Amber	Amber	https://ambermd.org
ChimeraX	Pettersen et al., 2004	https://www.cgl.ucsf.edu/chimera/
Clampex10	Molecular Devices	https://www.moleculardevices.com
COOT	Emsley and Cowtan, 2004	https://www2.mrc-lmb.cam.ac.uk/personal/pemsley/coot
cryoSPARC	Punjani et al., 2017	https://cryosparc.com
CTFFIND4	Rohou and Grigorieff, 2015	https://grigoriefflab.umassmed.edu/ctffind4
Gautomatch	Gautomatch	http://www.mrc-lmb.cam.ac.uk/kzhang/
Gromacs v.2020.2	Pall et al., 2020	https://manual.gromacs.org/2020.2/index.html
HOLE	Smart et al., 1996	http://www.holeprogram.org
MotionCor2	Zheng et al., 2017	https://hpc.nih.gov/apps/MotionCor2.html
Origin Software	Malvern Instrument	http://www.originlab.com
Phenix	Liebschner et al., 2019	https://www.phenix-online.org
Prism v8.0	GraphPad Software	https://www.graphpad.com
PyMOL	Schrödinger	https://pymol.org/2/
RELION-3.1	Zivanov et al., 2018	https://www3.mrc-lmb.cam.ac.uk/relion/index.php?title=Main_Page
ResMap	Kucukelbir et al., 2014	http://resmap.sourceforge.net
SerialEM	Takaba et al., 2020	https://bio3d.colorado.edu/SerialEM/
Adobe Illustrator CC	Adobe	https://www.adobe.com

RESOURCE AVAILABILITY

Lead contact

Further information and requests for resources and reagents should be directed to and will be fulfilled by the lead contact Yuequan Shen (yshen@nankai.edu.cn).

Materials availability

All unique/stable reagents generated in this study are available from the lead contact with a completed materials transfer agreement.

Data and code availability

- Atomic coordinates and cryo-EM density maps have been deposited in the Protein Data Bank and the Electron Microscopy Data Bank, respectively. They are publicly available as of the date of publication. Accession numbers are listed in the key resources table.
- This paper does not report original code.
- Any additional information required to reanalyze the data reported in this paper is available from the lead contact upon request.

EXPERIMENTAL MODEL AND SUBJECT DETAILS

Human embryonic kidney HEK293T cells were obtained from the American Type Culture Collection (CRL-11268) and were not validated further. Human embryonic kidney HEK293S-GnTi cells were a gift from Professor Jun Liao from the University of Shanghai

Science and Technology and were not validated further. HEK293T cells were grown in a humidified 37°C incubator with 5% CO_2 using DMEM (Sigma, Cat# D5648) containing 10% fetal bovine serum (FBS, PAN-Seratech, Cat# ST30-3302). HEK293S-GnTi cells were cultured in Freestyle 293 medium (GIBCO, Cat# 12338-018) supplemented with 5% CO_2 in a humidified 37°C incubator.

African green monkey kidney COS-7 cells were a gift from the Laboratory of Professor Junjie Hu from the Institute of Biophysics, Chinese Academy of Science and were not validated further. COS-7 cells were grown in a humidified 37°C incubator with 5% CO_2 using DMEM (Sigma, Cat# D5648) containing 10% fetal bovine serum (FBS, PAN-Seratech, Cat# ST30-3302).

Spodoptera frugiperda (Sf9) cells were a gift from the Laboratory of Professor Xinquan Wang from Tsinghua University and were not validated further. Sf9 cells were grown at 27°C using Insect-XPRESS medium (Lonza BioWhittaker, Cat# 12-730Q).

METHODS DETAILS

Plasmid

The gene encoding *Homo sapiens* TACAN (UniProt: Q9BXJ8) was synthesized (Genewiz, Inc.) and cloned into the pEG-BacMam vector, with a 3C protease site and GFP tag at the C-terminus. This plasmid was used to generate baculovirus using the Bac-to-Mam baculovirus expression system (Invitrogen).

Protein expression and purification

The plasmid expressing wild-type hTACAN was transfected into DH10Bac cells to produce Bacmid. Adherent sf9 cells grown at 27°C were transfected with purified Bacmid to produce P1 virus. The P1 virus then infected the sf9 suspension cells at a 1:80 (v/v) ratio to produce P2 virus. HEK293S-GnTi cells were cultured in Freestyle 293 medium (GIBCO) supplemented with 5% CO_2 at 37°C. The cells were transfected with P2 virus of hTACAN at a 1:50 (v/v) ratio when the cell density reached 2×10^6 cells per ml. After 12 h, sodium butyrate was added to the cell culture at a final concentration of 10 mM and the temperature was adjusted to 30°C to facilitate protein expression. After 60 h, suspension cells were collected and stored at -80°C.

For protein purification, 1.5 liters of cells were resuspended in buffer containing 20 mM Tris-HCl pH 8.0 and 200 mM NaCl. The suspension was supplemented with 0.5% (w/v) lauryl maltose neopentyl glycol (LMNG, Anatrace), 0.1% (w/v) cholesteryl hemisuccinate tris salt (CHS, Anatrace) and 1× protease inhibitor cocktail (TagetMol). After lysis at 4°C for 2 h, the sample was ultracentrifuged for 50 min at 130,000×g and the supernatant was incubated with GFP-Trap Agarose (ChromoTek) at 4°C by gentle rotation for 2.5 h. The resin was washed with buffer containing 20 mM Tris-HCl pH 8.0, 200 mM NaCl, 0.01% (w/v) LMNG with 0.001% (w/v) CHS and 0.0033% (w/v) glycol-diosgenin (GDN, Anatrace) with 0.00033% (w/v) CHS. Afterwards, the hTACAN protein was eluted by incubating resin with rhinovirus 3C protease at a ratio of 1:40 (v/v) to cleave the GFP tag overnight. The eluent was then concentrated to 1 mL using a 100 kDa cutoff concentrator (Millipore) and further purified with superose 6 10/300 GL (GE Healthcare), which was equilibrated with buffer containing 20 mM Tris-HCl pH 8.0, 200 mM NaCl, 0.00075% (w/v) LMNG and 0.00025% (w/v) GDN. The peak fractions were pooled and concentrated to 25 mg/mL for cryo-EM grid preparation.

Cryo-EM sample preparation

An aliquot of 2 μL purified hTACAN was placed on a glow-discharged holey carbon film gold grid (Protochips, CF-2/1, 200 mesh). The grid was blotted at 8°C and 100% humidity and plunge-frozen in liquid ethane using FEI Vitrobot Mark IV (Thermo Fisher Scientific). Cryo-EM data were collected on a Titan Krios electron microscope operated at an acceleration voltage of 300 kV with a defocus range of -1.0 μm to -2.0 μm using SerialEM software (Takaba et al., 2020). Micrographs were recorded by a Gatan K2 Summit direct electron detector in super-resolution mode with a pixel size of 0.507 Å (a physical pixel size of 1.014 Å) with a dose rate of 7.2 electrons per pixel per second for a total exposure time of 8 s, resulting in an image stack with 40 frames.

Image processing

A total of 2,585 image stacks were collected and subjected to beam-induced motion correction using MotionCor2 (Zheng et al., 2017) with binning to physical pixel size. The contrast transfer function (CTF) parameters for each micrograph were estimated using CTFFIND4 (Rohou and Grigorieff, 2015) on the basis of summed images without dose-weighting. Micrographs of low quality were excluded manually according to the CTF power spectra and summed images in Relion-3.1 (Zivanov et al., 2018). A total of 682,480 particles from 2,068 micrographs were picked semiautomatically using Gautomatch (http://www.mrc-lmb.cam.ac.uk/kzhang/). Two rounds of 2D classification were performed to exclude noise and poorly defined particles using Relion-3.1. The well-defined subsets accounting for 369,479 particles were extracted in Relion-3.1 and then used to generate an initial model through the *Ab initio* reconstruction in CryoSPARC-2 (Punjani et al., 2017). The initial model was low passed to 30 Å resolution for the first round of 3D classification in Relion-3.1. After 2 rounds of 3D classification (3 expected classes in each round), 64,446 particles were selected and subsequently subjected to 3D refinement and Bayesian polishing in Relion-3.1. The polished particles were then imported to CryoSPARC-2 for heterogeneous refinement and nonuniform refinement, and a final map at 3.66 Å resolution was produced from 58,843 particles with C2 symmetry imposed. The final resolution was estimated based on the gold-standard Fourier shell correlation (0.143 criteria) after correction for the use of masks. The local resolution map was calculated using ResMap (Kucukelbir et al., 2014) and exhibited using UCSF Chimera (Pettersen et al., 2004). Data collection and reconstruction workflow are shown in Figure S1.

Model building and refinement

The atomic model of hTACAN was manually built in COOT software (Emsley and Cowtan, 2004), sequence assignment was mainly guided by secondary structure prediction results from PSIPRED Workbench (Jones, 1999) and visible densities of residues with bulky side chains (Trp, Phe, Tyr and Arg) and refined using the real-space refinement in Phenix (Liebschner et al., 2019). The quality of the final model was validated using the module 'Comprehensive validation (cryo-EM)' in Phenix. Refinement and validation statistics are provided in Table S1. The figures showing structures were generated by the UCSF ChimeraX package (Pettersen et al., 2004), UCSF Chimera and PyMol (Schrödinger, USA).

Co-immunoprecipitation

Transfected HEK293T cells were washed twice with Tris-buffered saline (TBS) and lysed in buffer containing 20 mM Tris-HCl (pH 8.0), 200 mM NaCl, 1% (w/v) n-dodecyl-β-D-maltopyranoside (DDM, Anatrace), 0.2% (w/v) CHS, and 1 × protease inhibitor cocktail (TargetMol). After incubation at 4°C for 1 h, cell lysates were centrifuged at 120,000 ×g for 40 min at 4°C. The supernatant was divided into two equal parts. One part was incubated with GFP-Trap Agarose (20 μL slurry, ChromoTek), and the other was incubated with anti-flag affinity beads (20 μL slurry, BioLegend) for 2-3 h at 4°C. The beads were washed five times with buffer containing 20 mM Tris-HCl (pH 8.0), 200 mM NaCl, 0.025% (w/v) DDM, and 0.005% (w/v) CHS and eluted with 40 μL gel-loading buffer. Then, 5 μL of the eluate was loaded onto 12% SDS-PAGE gels and transferred to a PVDF membrane for western blot analysis.

Cell surface biotinylation assay

The transfected HEK293T cells were washed twice with ice-cold 1×PBS and then treated with 1 mg/mL biotinamidohexanoic acid 3-sulfo-N-hydroxysuccinimide ester sodium salt in PBS for 40 min at 4°C. Then, the cells were washed with ice-cold buffer containing 20 mM Tris-HCl (pH 8.0) and 200 mM NaCl and incubated at room temperature for 15 min. Cells were collected by scraping and lysed in buffer containing 20 mM Tris-HCl (pH 8.0), 200 mM NaCl, 1% (w/v) DDM, 0.2% (w/v) CHS, and 1 × protease inhibitor cocktail. After incubation at 4°C for 1 h, cell lysates were centrifuged at 120,000 ×g for 40 min at 4°C. Each sample of supernatant was incubated with 40 μL of 50% NeutrAvidin agarose (Thermo Fisher) at 4°C overnight. The beads were then washed three times with buffer containing 20 mM Tris-HCl (pH 8.0), 200 mM NaCl, 0.025% (w/v) DDM, and 0.005% (w/v) CHS and eluted by incubation with 80 μL gel-loading buffer at 37°C for 30 min. Then, 10 μL of the eluate was loaded onto 12% SDS-PAGE gels and transferred to a PVDF membrane for western blot analysis.

Electrophysiology

COS-7 cells were transiently transfected with wild-type or mutant TACAN-GFP for 24 to 48 h at 37°C with 5% CO_2. Transfected cells were then digested by trypsin to be plated onto 35-mm dishes for cultivation for at least 3 h before electrophysiology. For the cell-attached recordings, the membrane voltage was held at -80 mV. The electrode holder was directly connected to a high-speed pressure clamp and pressure-vacuum pump (HSPC, ALA Scientific). The pressure pulse was delivered through the recording electrode directly. Each cell membrane patch was subjected to 16 sweeps (the steady pressure of each scan lasts for 500 ms) of incrementally increasing negative pressure from 0 mmHg to -150 mmHg at -10 mmHg increments. Cell-attached currents were amplified with an Axopatch 200B and digitized with a Digidata 1550A system (Molecular Devices, Sunnyvale). All currents were sampled at 10 kHz and low-pass filtered at 0.5 kHz through pCLAMP software. For cell-attached recordings, both the extracellular bath solution and the pipette solution consisted of the following (in mM): NaCl 140, KCl 5, $CaCl_2$ 2, $MgCl_2$ 2, HEPES 10 and glucose 10 (pH adjusted to 7.4 with NaOH, 305 mOsm).

Cross-linking experiment

The purified hTACAN wild-type and mutant proteins (approximately 2 μg each) were cross-linked with 25 μM disuccinimidyl suberate (DSS) at room temperature for 30 minutes and then quenched with 20 mM Tis-HCl pH 8.0. The samples were then analyzed by SDS-PAGE, followed by Western blot analysis with the anti-FLAG antibody.

Coarse-grained MD simulations

Coarse-grained MD simulations were performed by using the Gromacs v.2020.2 program (Pall et al., 2020). The protein coordinates of dimeric hTACAN were embedded in a 125 Å× 125 Å bicomponent bilayer composed of POPC and cholesteric (4:1) using the insane script (Wassenaar et al., 2015). The ElNeDyn elastic network (Periole et al., 2009) was applied to the protein. The system was solvated by nonpolarizable water and neutralized at 0.15 M NaCl and 0.02 M $CaCl_2$ concentrations. The size of the simulation box was 125 Å× 125 Å × 180 Å. The Martini force field version 2.2 was used for protein, and the version 2.0 force field was used for POPCs, cholesterols, and ions (Jong et al., 2013). By using a velocity-rescaling thermostat (Bussi et al., 2007) with coupling constants of τ_T = 1.0 ps, the temperature was maintained at 310 K. The pressure was controlled at 1 bar by the Berendsen thermostat (Berendsen et al., 1984) with a coupling constant of τ_P=1.0 ps. The type of constraint applied to bonds was the LINCS algorithm (Hess et al., 1998). A Verlet cutoff scheme was used, and the PME method (Darden et al., 1993) was applied to calculate long-range electrostatic interactions. Periodic boundary conditions were used in the x-, y- and z-directions. The time step was set to 20 fs. Three independent production phases were performed, and each production phase replicate was run for 1 μs.

All-atom MD simulations

The final frames of the coarse-grained simulations were selected as the template to build the all-atom model system. The following steps were performed to provide the starting coordinates for all-atom MD: (i) the hTACAN-POPC-water system was transformed from the coarse-grained simulations above to the all-atom model using the backward.py protocol (Wassenaar et al., 2014), (ii) the backward-generated hTACAN was replaced with the cryo-EM hTACAN structure after aligning the main chain of them, and (iii) the overlapped lipids and water molecules were removed through the operations in VMD (Humphrey et al., 1996). In the hTACAN-POPC-water system, the protonation state for titratable residues of protein was determined using the H++ program (Anandakrishnan et al., 2012). For the titratable residues of the hTACAN protein, all Asp and Glu are deprotonated, Lys and Cys residues are protonated, and His residues are neutral with a proton on the Nδ nitrogen. Except for the residues His197, His330, His331 and His312, they are neutral with a single proton on the Nε nitrogen. The missing atoms were added automatically using the Tleap module in AMBER 20 (http://ambermd.org/AmberMD.php). All proteins were capped at the N- and C-termini with acetyl and methylamide groups, respectively. The size of the all-atom system was initially measured as 123 Å× 123 Å × 177 Å, for a total of 270001 atoms.

All-atom MD simulations were carried out using AMBER 20 with the PMEMD engine (http://ambermd.org/AmberMD.php). The AMBER FF14SB force field (Maier et al., 2015) was used for proteins, and the AMBER lipid force field LIPID14 (Dickson et al., 2014) was used for POPCs and cholesterols. A 12 Å cutoff was set for the nonbonded interaction. The SHAKE algorithm (Ryckaert et al., 1977) integration was used to constrain the covalent bonds involving hydrogen atoms, and the particle mesh Ewald (PME) algorithm (Darden et al., 1993) was applied to treat long-range electrostatic interactions. First, the system was minimized for 10,000 steps. Second, each system was heated from 0 K to 310 K in 500 ps using the Langevin thermostat (Pastor et al., 1988), and the proteins and lipids were constrained with a force constant of 50 kcal·mol^{-1}·Å^{-2}. Third, a series of equilibrations were performed for each system, and the lipids were equilibrated for 30 ns with the proteins constrained, followed by 10-ns equilibration without any constraint applied for the entire system. Finally, a 200-ns production phase was performed for the all-atom system. The time step was set to 2 fs. The frames were saved every 5,000 steps for analysis.

By using the surface tension regulation in AMBER 20 (http://ambermd.org/AmberMD.php), a constant surface tension was applied to the membrane surface (xy plane), and periodic boundary conditions and semi-isotropic pressure scaling were applied in the system. After the above minimization, heating and equilibration phases, three independent 200-ns production phases were performed at different surface tension values (without, 25, 30, and 35 mN/m for wild type hTACAN dimer; without and 35 mN/m for mutant M207A dimer). All other simulation parameters were set to the same as above.

Liquid chromatography–mass spectrometry (LC–MS)

Purified hTACAN proteins were mixed with methanol and chloroform. The mixture was vortexed and incubated at room temperature for 15 min and then centrifuged at 14,000 ×g for 10 min. The aqueous layer on the top and the protein pellet layer in the middle were removed and discarded, and the bottom chloroform layer was transferred into a new 1.5 mL tube and dried under vacuum. The dried extract was dissolved in 80 μL methanol with 0.1% formic acid for LC–MS analysis.

QUANTIFICATION AND STATISTICAL ANALYSIS

Data were analyzed using the GraphPad Prism 7 software with parametric or non-parametric statistical tests. No specific randomization or blinding protocol was used. Results are presented as the mean ± standard error of the mean (SEM) of at least three independent experiments. The sample size was chosen according to common practice in patch clamp experiments. The number (n) of independent experiments is indicated throughout the manuscript and shown in figures.